Progress In Electromagnetics Research C, Vol. 133, 97–107, 2023

Adaptive Anisotropy Optimization Method for the Radial Point Interpolation Method in Lossy Media

Hichem Naamen[1, *], Ajmi B. H. Hamouda[2], and Taoufik Aguili[1]

Abstract—In this paper, we present a new numerical anisotropy optimization method for the three-dimensional (3D) radial point interpolation method (RPIM) in lossy media. In classical optimization algorithms, the parameters of the artificial anisotropy or the scaling factors are usually evaluated along the selected axes. Instead, once the analytical expressions of these adaptive factors have been determined, they are assigned at each node through their shape functions. By adaptive factor, we mean that its value varies in such a way to cancel the discrepancy between numerical and exact wavenumbers at each node. Doing such optimization at each node is indeed possible during the calculation of these parameters by the RPIM dispersion relation. Therefore, the numerical anisotropy is no longer optimized by averaging over the entire Cartesian grid but rather over each node direction. The RPIM numerical anisotropy adaptive optimization method (AOM) in lossy media is presented, and the theoretical adaptive factors are given as functions of node positions. Our results show that optimizing with the AOM considerably reduces the numerical errors of the dispersion and anisotropy. The proposed AOM scheme is applied to a 3D rectangular cavity in order to test its validity and evaluate the accuracy of the numerical results of our approach.

1. INTRODUCTION

Mesh-based methods, such as the finite element method (FEM), method of moments (MoM), and finite difference time domain method (FDTD), solve Maxwell's equations by segmenting the computational domain into connected sub-domains of simple shapes and discrete time steps to establish the system of algebraic equations [1]. In spite of the vast performance from these methods, the meshes/grids needed to generate polygons for complex geometries restrict their applications, influence precision, and increase computational time due to continuity relations connecting these meshes [2].

Alternatively, meshless methods do not require topological relations between the nodes or continuity equations [3]. They lead to multiscale node distributions [4] and adaptive refinement to increase simulation accuracy [5]. Among them are the smoothed particle electromagnetic method (SPEM) [6], partition of unity method (PUM) [7], and meshless local Petrov-Galerkin method (MLPGM) [8]. These methods have been improved to overcome the limitations of mesh methods and solve complex problems.

In the absence of analytical solutions of Maxwell's equations for complex geometries, and since numerical methods cannot incorporate the actual continuum in space and time, the discretization process is an alternative solution for modelling electromagnetic phenomena. However, the inevitable drawback is that such discretization generates numerical dispersion which induces distortions in the waveforms. Moreover, the phase error is anisotropic since it depends on the direction of the waveforms, which are slightly cubical [9] rather than spherical. In addition, numerical dispersion causes cumulative phase error leading to resonance mislocations in the frequency domain.

Received 15 March 2023, Accepted 12 May 2023, Scheduled 27 May 2023
* Corresponding author: Hichem Naamen (naamen.hichem123@gmail.com).
[1] National Engineering School at Tunis, Technology Department of Information and Communications, Tunisia. [2] Quantum and Statistical Physics Laboratory, Faculty of Sciences, University of Monastir, Tunisia.

To rectify the problem of numerical dispersion, several techniques have been proposed within the framework of meshing methods [10, 11]. Artificial anisotropy was implemented to reduce dispersion error [9]. Cole has introduced the non-standard finite-difference (NSFD) formulation [12] and Forgy and Chew created an algorithm based on the linear superposition of two lattices [13]. It should be pointed out that the implementation of these schemes is not compatible with the standard FDTD algorithm except for the NSFDTD. In summary, the numerical anisotropy optimization is limited by the finite-difference scheme to approximate the curl.

On the other hand, the RPIM algorithm numerically processes the shape functions to handle topological node connectivity information, and the unknown fields are expanded over these shape functions. Thus, for the curls in Maxwell's equations for the corresponding EM fields are replaced by their expanded shape-function derivatives. The RPIM algorithm is an accurate alternative to estimate the spatial curl in Maxwell's equations by avoiding the finite-difference scheme, the pedestal of the FDTD discretization process.

In this paper, a simple adaptive technique which significantly reduces both of the dispersion error and the numerical anisotropy for 3D-RPIM in lossy media is proposed. Our approach is based on an extended procedure with a new formulation of the algorithm, described as follows: 1) to adjust the numerical dispersion for the exact known value, the scaling factors are calculated analytically from the RPIM dispersion relation; 2) the scaling factors are discretized and expressed as a function of (i, j, k) node position; 3) the E/H shape functions are computed with the associated discretized scaling factors at each node position in accordance with Maxwell's equations; 4) a diagonal matrix containing the scaling factors according to the transition matrix is computed. In Section 2, RPIM Maxwell's equations in lossy media are given. In Section 3, the formulation of the AOM is detailed. In Sections 4 and 5, numerical and experimental results are presented to confirm and validate the proposed AOM accuracy.

2. RPIM MAXWELL'S EQUATIONS IN LOSSY MEDIA

To implement the meshless RPIM technique in three dimensions, one must define two complementary sets of electric field nodes (E-nodes) and magnetic field nodes (H-nodes). However, in contrast to the FDTD method, all three components of the electric field are placed at the same E-node. The same applies to the magnetic field. The coupling aspect of electromagnetic field components requires that each E-node should be surrounded by H-nodes and vice-versa [14].

In this paper, E- and H-nodes are spread similarly to the point-matched time-domain finite-element method [15]. Hence, each (i, j, k) E-node is surrounded by eight H-nodes, four at each of the $(k - 1/2)$ and $(k + 1/2)$ planes. Thus, we have selected eight surrounding H-nodes in the E-node support domain and vice versa [16]. The ideal distribution of nodes is corresponding to a large number of nodes per support domain, but such a large number will increase the computational cost through the corresponding shape functions. For 3D problems, the minimal number of nodes per support domain is eight [Fig. 6] while there are four for 2D problems. As opposed to the FDTD, RPIM grids match the edge of the curve and avoid the discontinuity problem encountered in the FDTD (at the staircase). Once the dual node distributions have been generated in the 3D domain, the E/H shape functions with their derivatives are numerically computed. Thus, eight H-node fields belonging to the E-node support domain will update the E-node field and vice versa [16]. The topological node connectivity is handled by processing their shape functions with minimal loss of geometric information.

A sourceless region with linear, isotropic, non-dispersive, and lossy media is considered. In Cartesian coordinates, the time-dependent 3D Maxwell's curl equations in differential form write:

$$\nabla \wedge \vec{H} = \overline{\overline{M}}_{\varepsilon} \frac{\partial \vec{E}}{\partial t} + \overline{\overline{M}}_{\sigma} \vec{E}, \tag{1}$$

$$\nabla \wedge \vec{E} = -\overline{\overline{M}}_{\mu} \frac{\partial \vec{H}}{\partial t} - \overline{\overline{M}}_{\sigma^*} \vec{H}. \tag{2}$$

Here $\overline{\overline{M}}_{\varepsilon} = \overline{\overline{\text{diag}}}\{\varepsilon_x, \varepsilon_y, \varepsilon_z\}$, $\overline{\overline{M}}_{\mu} = \overline{\overline{\text{diag}}}\{\mu_x, \mu_y, \mu_z\}$, $\overline{\overline{M}}_{\sigma} = \overline{\overline{\text{diag}}}\{\sigma_x, \sigma_y, \sigma_z\}$ and $\overline{\overline{M}}_{\sigma^*} = \overline{\overline{\text{diag}}}\{\sigma_x^*, \sigma_y^*, \sigma_z^*\}$ are diagonal matrices with positive real elements composed of the permittivity ε, the permeability μ, the electric conductivity σ, and the equivalent magnetic loss σ^*.

A second-order centered difference may approximate $[\partial\vec{E}/\partial t]^{n+1/2}$ and $[\partial\vec{H}/\partial t]^{n}$ by $(\vec{E}^{n+1}-\vec{E}^{n})/\Delta t$ and $(\vec{H}^{n+1/2}-\vec{H}^{n-1/2})/\Delta t$, respectively, i.e., $\vec{E}^{n+1/2}$ and $\vec{H}^{n}$ are estimated with second-order accuracy using the averages of the electric field at time levels n and $n+1$, and the magnetic field at time levels $n-1/2$ and $n+1/2$, respectively [17]. After several rearrangements, $\vec{E}^{n+1}$ and $\vec{H}^{n+1/2}$ at the E/H-node of interest $X_i^{E/H}$ lead to the following equations:

$$\begin{aligned}\vec{E}^{n+1}(X_i^E) &= \left[2\overline{\overline{M}}_{\varepsilon}+\Delta t\overline{\overline{M}}_{\sigma}\right]^{-1}\left[2\overline{\overline{M}}_{\varepsilon}-\Delta t\overline{\overline{M}}_{\sigma}\right]\vec{E}^{n}(X_i^E)\\ &\quad +2\Delta t\left[2\overline{\overline{M}}_{\varepsilon}+\Delta t\overline{\overline{M}}_{\sigma}\right]^{-1}\left\{\nabla\wedge\vec{H}^{n+1/2}\right\}(X_i^E), \qquad (3)\\ \vec{H}^{n+1/2}(X_i^H) &= \left[2\overline{\overline{M}}_{\mu}+\Delta t\overline{\overline{M}}_{\sigma^*}\right]^{-1}\left[2\overline{\overline{M}}_{\mu}-\Delta t\overline{\overline{M}}_{\sigma^*}\right]\vec{H}^{n-1/2}(X_i^H)\\ &\quad -2\Delta t\left[2\overline{\overline{M}}_{\mu}+\Delta t\overline{\overline{M}}_{\sigma^*}\right]^{-1}\left\{\nabla\wedge\vec{E}^{n}\right\}(X_i^H). \qquad (4)\end{aligned}$$

where $\vec{H}^{n+1/2}$ and $\vec{E}^{n}$ components are interpolated over the H/E-shape functions inside their associate local support domains [18], leading to:

$$\left\{\nabla\wedge\vec{E}^{n}\right\}(X_i^H)=\sum_{j=1}^{j=N}\left\{\nabla\wedge\phi_j^E\right\}(X_i^H)\vec{E}_j^{n}=\overline{\overline{C}}_E\vec{E}^{n}, \qquad (5a)$$

$$\left\{\nabla\wedge\vec{H}^{n+1/2}\right\}(X_i^E)=\sum_{j=1}^{j=N}\left\{\nabla\wedge\phi_j^H\right\}(X_i^E)\vec{H}_j^{n+1/2}=\overline{\overline{C}}_H\vec{H}^{n+1/2}, \qquad (5b)$$

with

$$\overline{\overline{C}}_E=\begin{pmatrix}\overline{\overline{0}}^{E} & -\overline{\overline{\phi}}_z^{E} & \overline{\overline{\phi}}_y^{E}\\ \overline{\overline{\phi}}_z^{E} & \overline{\overline{0}}^{E} & -\overline{\overline{\phi}}_x^{E}\\ -\overline{\overline{\phi}}_y^{E} & \overline{\overline{\phi}}_x^{E} & \overline{\overline{0}}^{E}\end{pmatrix},\quad \overline{\overline{C}}_H=\begin{pmatrix}\overline{\overline{0}}^{H} & -\overline{\overline{\phi}}_z^{H} & \overline{\overline{\phi}}_y^{H}\\ \overline{\overline{\phi}}_z^{H} & \overline{\overline{0}}^{H} & -\overline{\overline{\phi}}_x^{H}\\ -\overline{\overline{\phi}}_y^{H} & \overline{\overline{\phi}}_x^{H} & \overline{\overline{0}}^{H}\end{pmatrix}, \qquad (6)$$

the superscript n is a temporal index; $\overline{\overline{0}}^{E/H}$ is the null matrix of appropriate dimensions; $\overline{\overline{C}}_E$ and $\overline{\overline{C}}_H$ are block matrices computed during the RPIM algorithm implementation and thoroughly described in [16]. The elements $\overline{\overline{\phi}}_{\xi}^{E/H}$ of $\overline{\overline{C}}_E/\overline{\overline{C}}_H$ are matrices collecting spatial E/H shape function derivatives for $\xi=x,y$, or z, for spread E/H nodes, evaluated at different $X_i^{H/E}$ nodes, respectively, and defined as:

$$\left[\phi_{\xi}^{E/H}\right]_{i,j}=\partial_{\xi}\phi_j^{E/H}(X_i^{H/E}). \qquad (7)$$

After some algebraic manipulations, we cast Equations (3) and (4) into more compact vector-matrix form as:

$$\vec{E}^{n+1}=\overline{\overline{A}}_1\vec{E}^{n}+\overline{\overline{A}}_2\overline{\overline{C}}_H\cdot\vec{H}^{n+1/2}, \qquad (8)$$

$$\vec{H}^{n+1/2}=\overline{\overline{B}}_1\vec{H}^{n-1/2}-\overline{\overline{B}}_2\overline{\overline{C}}_E\cdot\vec{E}^{n}, \qquad (9)$$

$\overline{\overline{A}}_1$, $\overline{\overline{A}}_2$, $\overline{\overline{B}}_1$, and $\overline{\overline{B}}_2$ are constant diagonal matrices, expressed as:

$$\overline{\overline{A}}_1=\left[2\overline{\overline{M}}_{\varepsilon}+\Delta t\overline{\overline{M}}_{\sigma}\right]^{-1}\left[2\overline{\overline{M}}_{\varepsilon}-\Delta t\overline{\overline{M}}_{\sigma}\right],\quad \overline{\overline{B}}_1=\left[2\overline{\overline{M}}_{\mu}+\Delta t\overline{\overline{M}}_{\sigma^*}\right]^{-1}\left[2\overline{\overline{M}}_{\mu}-\Delta t\overline{\overline{M}}_{\sigma^*}\right], \qquad (10a)$$

$$\overline{\overline{A}}_2=2\Delta t\left[2\overline{\overline{M}}_{\varepsilon}+\Delta t\overline{\overline{M}}_{\sigma}\right]^{-1},\qquad \overline{\overline{B}}_2=2\Delta t\left[2\overline{\overline{M}}_{\mu}+\Delta t\overline{\overline{M}}_{\sigma^*}\right]^{-1}. \qquad (10b)$$

Substituting Equation (9) into (8) yields:

$$\vec{E}^{n+1}=\left[\overline{\overline{A}}_1-\overline{\overline{A}}_2\overline{\overline{B}}_2\overline{\overline{C}}_H\overline{\overline{C}}_E\right]\vec{E}^{n}+\overline{\overline{A}}_2\overline{\overline{B}}_1\overline{\overline{C}}_H\vec{H}^{n-1/2}, \qquad (11)$$

$$\vec{H}^{n+1/2}=-\overline{\overline{B}}_2\overline{\overline{C}}_E\cdot\vec{E}^{n}+\overline{\overline{B}}_1\vec{H}^{n-1/2}, \qquad (12)$$

$$\vec{\psi}^{n+1}=\overline{\overline{G}}\cdot\vec{\psi}^{n}, \qquad (13)$$

Equations (11) and (12) are combined into Equation (13), in matrix form, where $\vec{\psi}^n = [\vec{E}^n, \vec{H}^{n-1/2}]^{\mathrm{T}} = [\vec{E}_x^n, \vec{E}_y^n, \vec{E}_z^n, \vec{H}_x^{n-1/2}, \vec{H}_y^{n-1/2}, \vec{H}_z^{n-1/2}]^{\mathrm{T}}$ and $\overline{\overline{G}}$ is the transition matrix defined by:

$$\underset{\sigma\neq 0,\,\sigma^*\neq 0}{\overline{\overline{G}}} = \begin{pmatrix} \overline{\overline{A}}_1 - \overline{\overline{A}}_2\overline{\overline{B}}_2\overline{\overline{C}}_H\overline{\overline{C}}_E & \overline{\overline{A}}_2\overline{\overline{B}}_1\overline{\overline{C}}_H \\ -\overline{\overline{B}}_2\overline{\overline{C}}_E & \overline{\overline{B}}_1 \end{pmatrix}, \quad \underset{\sigma\neq 0,\,\sigma^*=0}{\overline{\overline{G}}} = \begin{pmatrix} \overline{\overline{A}}_1 - \Delta t\overline{\overline{A}}_2\overline{\overline{M}}_\mu^{-1}\overline{\overline{C}}_H\overline{\overline{C}}_E & \overline{\overline{A}}_2\overline{\overline{C}}_H \\ -\Delta t\overline{\overline{M}}_\mu^{-1}\overline{\overline{C}}_E & \overline{\overline{I}}_3 \end{pmatrix}, \quad (14)$$

where $\overline{\overline{I}}_n$ is the $n \times n$ identity matrix.

3. FORMULATION OF THE PROPOSED AOM

3.1. Scaling Factors versus Propagation Angle

The 3D-RPIM dispersion relation for a lossy media given in [18] writes:

$$\sin^2\left(\frac{\omega\Delta t}{2}\right) - \frac{\sigma\sigma^*\left(\Delta t\right)^2}{4\varepsilon\mu}\cos^2\left(\frac{\omega\Delta t}{2}\right) - j\left(\frac{\sigma\Delta t}{4\varepsilon} + \frac{\sigma^*\Delta t}{4\mu}\right)\sin\left(\omega\Delta t\right) = S^2\Psi\left(k_{\mathrm{num}}\right), \quad (15)$$

here, the Courant factor is $S = c\Delta t/\Delta$, with $c = 1/\sqrt{\varepsilon\mu}$ the speed of light in the modeled media, $\Delta = \Delta x = \Delta y = \Delta z = \lambda_0/N_s$ the uniform spatial resolution, λ_0 the exact wavelength in the lossy material, N_s the spatial sampling rate, ω the angular frequency, and Δt the time step size.

$$W_x = \sin\left(\frac{k_x\Delta x}{2}\right)\cos\left(\frac{k_y\Delta y}{2}\right)\cos\left(\frac{k_z\Delta z}{2}\right), \quad W_y = \cos\left(\frac{k_x\Delta x}{2}\right)\sin\left(\frac{k_y\Delta y}{2}\right)\cos\left(\frac{k_z\Delta z}{2}\right), \quad (16a)$$

$$W_z = \cos\left(\frac{k_x\Delta x}{2}\right)\cos\left(\frac{k_y\Delta y}{2}\right)\sin\left(\frac{k_z\Delta z}{2}\right), \quad \Psi(k) = W_x^2 + W_y^2 + W_z^2, \quad (16b)$$

where $k_x = k\sin(\theta)\cos(\phi)$, $k_y = k\sin(\theta)\sin(\phi)$, and $k_z = k\cos(\theta)$ are the three wavenumbers along the x, y, and z directions, respectively. Here k is the numerical wavenumber, and (ϕ, θ) are the azimuthal and polar angles in a spherical coordinate system, respectively. Δx, Δy, and Δz are the uniform distances between neighboring E/H-nodes in the corresponding directions.

As shown in [18], the numerical resolution of this dispersion relation is a set of complex numerical wavenumbers which are quite far from the exact values [19], which causes numerical dispersion and anisotropy. Under this form, Equation (15) cannot be verified for the exact wavenumber and consequently have to be scaled by (sc_1, sc_2) [20], and these scaling factors are inserted into the dispersion relation to adjust the numerical factor to the exact value. The scaling factors act on (ε, μ) and (σ, σ^*), respectively. Thus, Equation (15) should be written as:

$$\sin^2\left(\frac{\omega\Delta t}{2}\right) - \frac{\sigma\sigma^*\cdot sc_2^2\left(\Delta t\right)^2}{4\varepsilon\mu\cdot sc_1^2}\cos^2\left(\frac{\omega\Delta t}{2}\right) - j\left(\frac{\sigma\cdot sc_2\Delta t}{4\varepsilon\cdot sc_1} + \frac{\sigma^*\cdot sc_2\Delta t}{4\mu\cdot sc_1}\right)\sin\left(\omega\Delta t\right) = \frac{S^2}{sc_1^2}\Psi\left(k_{\mathrm{exact}}\right). \quad (17)$$

Equation (17) can be decomposed into two real equations by balancing the real and imaginary parts of both side of Equation (17), as all parameters in Equation (17) are real except k_{exact}. Equating real parts of two sides gives:

$$\sin^2\left(\frac{\omega\Delta t}{2}\right)\cdot sc_1^2 - \frac{\sigma\sigma^*\Delta t^2}{4\varepsilon\mu}\cos^2\left(\frac{\omega\Delta t}{2}\right)\cdot sc_2^2 = S^2\cdot\mathrm{Re}[\Psi\left(k_{\mathrm{exact}}\right)]. \quad (18)$$

Equating imaginary parts of two sides gives:

$$sc_1\cdot sc_2 = \frac{-4\varepsilon\mu S^2\cdot\mathrm{Im}\left[\Psi\left(k_{\mathrm{exact}}\right)\right]}{\left(\mu\sigma + \varepsilon\sigma^*\right)\cdot\Delta t\cdot\sin\left(\omega\Delta t\right)}. \quad (19)$$

The equations of the obtained nonlinear system can then be analytically solved for the scaling factors after some algebraic calculations and are expressed as:

$$\begin{aligned} sc_1 &= \frac{S\sqrt{\mathrm{Re}\left[\Psi\left(k_{\mathrm{exact}}\right)\right]}}{\sqrt{2}\sin\left(\frac{\omega\Delta t}{2}\right)}\sqrt{1+\sqrt{1+\frac{4\varepsilon\mu\sigma\sigma^*\mathrm{Im}^2\left[\Psi\left(k_{\mathrm{exact}}\right)\right]}{\left(\mu\sigma+\varepsilon\sigma^*\right)^2\mathrm{Re}^2\left[\Psi\left(k_{\mathrm{exact}}\right)\right]}}}, \\ sc_2 &= \left(\frac{-4\varepsilon\mu S^2\mathrm{Im}\left[\Psi\left(k_{\mathrm{exact}}\right)\right]}{\left(\mu\sigma+\varepsilon\sigma^*\right)\Delta t\sin\left(\omega\Delta t\right)}\right) \Big/ sc_1. \end{aligned} \quad (20)$$

For electrically lossy media ($\sigma^* = 0$), the scaling factors have the following expressions:

$$sc_1 = \frac{S}{\sin\left(\frac{\omega\Delta t}{2}\right)}\sqrt{\mathrm{Re}\left[\Psi\left(k_{\mathrm{exact}}\right)\right]}, \quad sc_2 = \frac{-2\varepsilon\tan\left(\frac{\omega\Delta t}{2}\right)}{\sigma\Delta t}\left(\frac{\mathrm{Im}\left[\Psi\left(k_{\mathrm{exact}}\right)\right]}{\mathrm{Re}\left[\Psi\left(k_{\mathrm{exact}}\right)\right]}\right)sc_1. \tag{21}$$

In the case of lossless media, we have $sc_2 = 0$. It must be noted that these scaling factors are functions of ϕ and θ and sweep the continuous space. Such a behavior cannot be handled numerically, unless the scaling factors are discretized and implemented by the AOM algorithm.

3.2. Scaling Factors versus Discrete Directions

The dispersion optimization techniques mentioned above use constant scaling factors, which are obtained by averaging over certain selected directions. The scaling factors as functions of azimuth and polar angles in a spherical coordinate system have to be expressed in Cartesian coordinates. This allows a dispersion optimization at every node of the grid. Instead of optimizing numerical dispersion along certain directions, it will be carried out for all grid directions that pass through E/H nodes. Hence, we will have to compute the shape functions taking into account these discretized and affected adaptive factors at each E/H node. The azimuthal and polar angles ϕ and θ in Cartesian coordinates can be written:

$$\phi[i,j] = \tan^{-1}\left(j\Delta y/i\Delta x\right), \quad \theta[i,j,k] = \cos^{-1}\left(k\Delta z\Big/\sqrt{(i\Delta x)^2 + (j\Delta y)^2 + (k\Delta z)^2}\right). \tag{22}$$

Let us define the dimensionless parameters as follows:

$$R = \Delta y/\Delta x, \quad Z = \Delta z/\Delta x. \tag{23}$$

After a simple calculation, we end up with:

$$\phi[i,j] = \tan^{-1}\left(Rj/i\right), \quad \theta[i,j,k] = \cos^{-1}\left(Zk\Big/\sqrt{i^2 + (Rj)^2 + (Zk)^2}\right), \tag{24}$$

$$\mathcal{A}_1[i,j,k] = \frac{S}{\sin\left(\frac{\omega\Delta t}{2}\right)}\sqrt{\mathrm{Re}[\Psi[i,j,k]]}, \quad \mathcal{A}_2[i,j,k] = \frac{-2\varepsilon\tan\left(\frac{\omega\Delta t}{2}\right)}{\sigma\Delta t}\left(\frac{\mathrm{Im}[\Psi[i,j,k]]}{\mathrm{Re}[\Psi[i,j,k]]}\right)\cdot sc_1[i,j,k]. \tag{25}$$

At this level, the discretized adaptive factors depend on the E/H-node positions. Hence, associated permittivities, permeabilities, and conductivities values are given by $\mathcal{A}_1[i,j,k] \times \varepsilon$, $\mathcal{A}_1[i,j,k] \times \mu$, and $\mathcal{A}_2 \times \sigma$ respectively, at (i,j,k) node positions.

3.3. Implementation into the RPIM Algorithm

For the sake of simplicity, let us consider only the case of electric losses. For the different optimization techniques mentioned in the introduction, $\overline{\overline{A}}_1$, $\overline{\overline{A}}_2$, $\overline{\overline{B}}_1$, and $\overline{\overline{B}}_2$ are constant diagonal matrices containing invariant optimized coefficients for all nodes. Regarding the proposed adaptive optimization technique, these coefficients retake values with respect to the environment of the considered node position. Their elements sweep all the E/H-nodes when being inserted into the matrices $\overline{\overline{C}}_E$ and $\overline{\overline{C}}_H$. Instead of first calculating the $\overline{\overline{C}}_E$ and $\overline{\overline{C}}_H$ matrices as illustrated in [16–18] and the coefficient matrices values affected during the implementation of the transition matrix $\overline{\overline{G}}$, the shape functions are simultaneously computed and associated with the appropriate elements of $\overline{\overline{A}}_2$ and $\overline{\overline{B}}_2$. To implement $\overline{\overline{A}}_1$, it would be adequate to construct a diagonal matrix which respects the numbering of nodes during the numerical implementation. Otherwise, the adaptive factors $sc_1[i,j,k]$ and $sc_2[i,j,k]$ ensure that k_{num} is equal to k_{exact} at the node (i,j,k) for arbitrary incident angles. On the other hand, if we assign constant values for the scaling factors according to certain directions, the dispersion error is only translated, but never canceled out. Hence, the AOM based on adaptive factors cancels the dispersion error under its two forms: phase error and also the loss one, and can be easily implemented without increasing the computational cost, thanks to the extensive flexibility of the RPIM algorithm.

Inserting Equation (5b) into (3) and replacing the coefficients by adaptive factors leads to:

$$\vec{E}^{n+1}(X_i^E) = C_1[l,m,n]\vec{E}^n(X_i^E) + C_2[l,m,n]\sum_{j=1}^{j=N}\left\{\nabla\wedge\phi_j^H\right\}(X_i^E)\vec{H}_j^{n+1/2}, \tag{26}$$

where X_i^E is the position of the ith E-node of coordinates (l, m, n), and:

$$C_1[l,m,n] = \frac{2\varepsilon \cdot \mathcal{A}_1[l,m,n] - \sigma \cdot \mathcal{A}_2[l,m,n]\Delta t}{2\varepsilon \cdot \mathcal{A}_1[l,m,n] + \sigma \cdot \mathcal{A}_2[l,m,n]\Delta t},$$
$$C_2[l,m,n] = \frac{2\Delta t}{2\varepsilon \cdot \mathcal{A}_1[l,m,n] + \sigma \cdot \mathcal{A}_2[l,m,n]\Delta t}, \tag{27}$$

$C_1[l, m, n]$ and $C_2[l, m, n]$ are not affected by the spatial derivatives since they only depend on the position; this gives:

$$\vec{E}^{n+1}(X_i^E) = C_1[l,m,n]\vec{E}^n(X_i^E) + \sum_{j=1}^{j=N} \left\{\nabla \wedge \left(C_2[l,m,n] \cdot \phi_j^H\right)\right\}(X_i^E)\vec{H}_j^{n+1/2}. \tag{28}$$

Hence, the $C_2[l, m, n]$ terms have to be inserted into the shape functions during the implementation of $\overline{\overline{C}}_H$.

Likewise, inserting Equation (5a) into (4) and replacing the coefficients by adaptive factors leads to:

$$\vec{H}^{n+1/2}(X_i^H) = C_1'[l,m,n]\vec{H}^{n-1/2}(X_i^H) - C_2'[l,m,n] \sum_{j=1}^{j=N} \left\{\nabla \wedge \phi_j^E\right\}(X_i^H)\vec{E}_j^n, \tag{29}$$

where X_i^H is the position of the ith H-node of coordinates (l, m, n), and:

$$C_1'[l,m,n] = \frac{2\mu \cdot \mathcal{A}_1[l,m,n] - \sigma^* \cdot \mathcal{A}_2[l,m,n]\Delta t}{2\mu \cdot \mathcal{A}_1[l,m,n] + \sigma^* \cdot \mathcal{A}_2[l,m,n]\Delta t},$$
$$C_2'[l,m,n] = \frac{2\Delta t}{2\mu \cdot \mathcal{A}_1[l,m,n] + \sigma^* \cdot \mathcal{A}_2[l,m,n]\Delta t}, \tag{30}$$
$$\vec{H}^{n+1/2}(X_i^H) = C_1'[l,m,n]\vec{H}^{n-1/2}(X_i^H) - \sum_{j=1}^{j=N} \left\{\nabla \wedge \left(C_2'[l,m,n] \cdot \phi_j^E\right)\right\}(X_i^H)\vec{E}_j^n, \tag{31}$$

the same procedure is repeated for $C_2'[l, m, n]$ terms which are inserted into the shape functions during the implementation of $\overline{\overline{C}}_E$.

4. NUMERICAL RESULTS AND VALIDATIONS

The RPIM dispersion and anisotropy characteristics in lossy media are given by:

$$\text{NPE} = \frac{\beta - \beta_0}{\beta_0}, \ \text{NLE} = \frac{\alpha - \alpha_0}{\alpha_0}, \ A_d = \frac{\beta_{\max} - \beta_{\min}}{\beta_{\min}}, \ A_l = \frac{\alpha_{\max} - \alpha_{\min}}{\alpha_{\min}}, \tag{32}$$

where β and β_0 are the numerical and physical phase constants; α and α_0 are the numerical and physical loss constants; A_l is the numerical anisotropy loss; A_d is the anisotropy dispersion; $\alpha_{\max}$ and $\beta_{\max}$ are the maxima of numerical loss constant and phase constant when scanning ϕ and θ; and $\alpha_{\min}$ and $\beta_{\min}$ are the minima, respectively.

Similar to the range used in [21], the conductivity is selected to vary from 10^{-4} S/m to 10^{0} S/m, thereby including the electric conductivity of most dielectric materials [22]. The operating frequency of the wave we are interested in is set to $f = 300$ MHz; nevertheless, our results are extrapolated to a larger frequency range.

Figures 1 and 2 show the numerical phase error (NPE) and the numerical loss error (NLE) versus ϕ for $\theta = 22.5°$, $\theta = 45°$, and $\theta = 45°$. The node sampling rate $N_s = 30$, the CFL number $S_{3D} = 0.5$, and conductivity $\sigma = 0.1$ S/m. In the classical axial optimization method, the values of the scale factors are calculated on the axes of the Cartesian coordinate system and are: $sc_1 = 1.0622$ and $sc_2 = 0.9360$. In such a method, the phase and loss errors are reduced by up to half compared to RPIM ones. However, the AOM cancels the NPE and NLE as shown in the bottom of Figures 1 and 2 for all θ values.

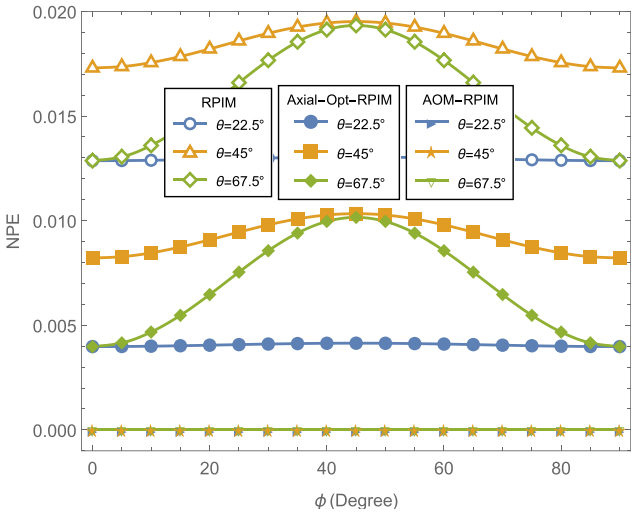

Figure 1. Numerical phase error for RPIM, axial optimized RPIM and AOM-RPIM with $\sigma = 0.1\,\mathrm{S/m}$, $N_s = 30$ and $S = 0.5$.

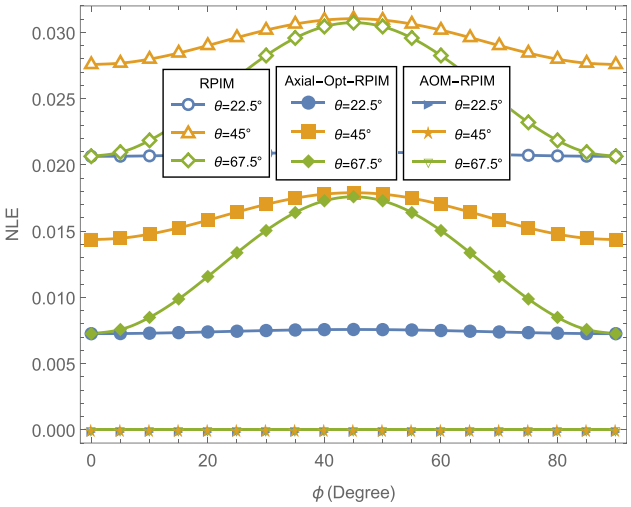

Figure 2. Numerical loss error for RPIM, axial optimized RPIM and AOM-RPIM with $\sigma = 0.1\,\mathrm{S/m}$, $N_s = 30$ and $S = 0.5$.

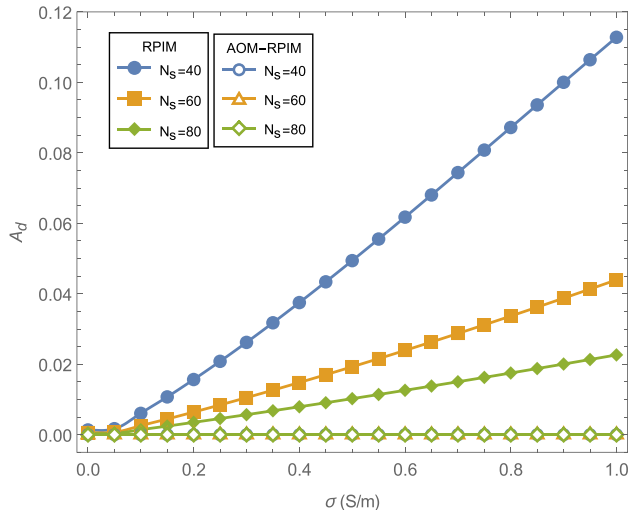

Figure 3. Anisotropy dispersion versus conductivity for RPIM and AOM-RPIM with $S = 0.5$, $N_s = 40$, $N_s = 60$ and $N_s = 80$.

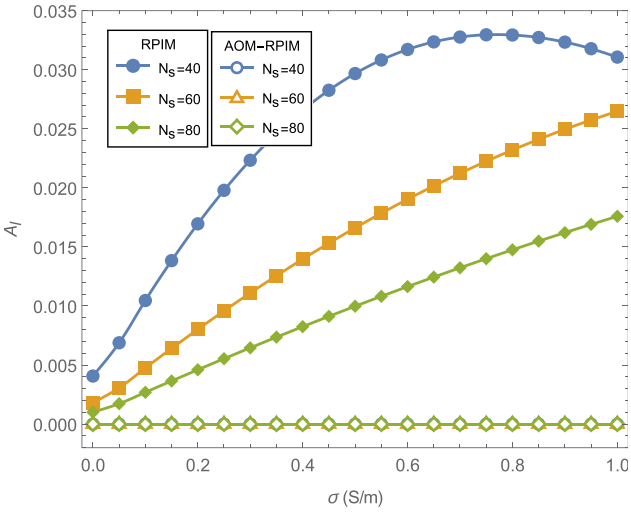

Figure 4. Anisotropy loss versus conductivity for RPIM and AOM-RPIM with $S = 0.5$.

In summary, NPE decreases from nearly 0.01 for the RPIM to 0.001 for the Axial-Opt-RPIM and completely canceled for AOM-RPIM whatever the ϕ values.

Figures 3 and 4 present A_d and A_l versus electric conductivity σ for $N_s = 40$, $N_s = 60$, and $N_s = 80$. Indeed, it is predictable that the anisotropy dispersion increases with σ and decreases with N_s, but for the AOM-RPIM, A_d and A_l are fully canceled (to much lower than 10^{-7}).

5. NUMERICAL EXPERIMENTS

To further validate the accuracy of the proposed method, even in the case of higher numerical anisotropy during the numerical experiments, the spatial sampling rate is fixed to $N_s \simeq 20$ at $f = 3.5\,\mathrm{GHz}$. A $3D$ rectangular cavity with dimensions $52\,\mathrm{mm} \times 40\,\mathrm{mm} \times 24\,\mathrm{mm}$, filled with a homogeneous lossy

media, and terminated by PEC walls is considered. The origin is at the lower-left corner of the domain in the Cartesian directions. In a similar fashion to [15] and [16], the studied domain is uniformly discretized using double staggered E/H grids (Figures 5 and 6). The cavity is excited by a sinusoidal point source modulated by a time-dependent Gaussian function given by: $J_z(A,n) = \exp[-((n\Delta t - 4\sigma)/(\sqrt{2}\sigma))^2]\sin[2\pi f(n\Delta t - 4\sigma)]$ located at $A\,(16\,\text{mm}, 20\,\text{mm}, 12\,\text{mm})$. The width factor is $\sigma = 0.122\,\text{ns}$, the CFL number $S_{3D} = 0.5$, and the observation point is at $B\,(36\,\text{mm}; 20\,\text{mm}; 12\,\text{mm})$. A set of RPIM parameters, transcendentally introduced in the RPIM algorithm [18], are selected so that the shape parameter $\alpha = 2$, the maximum distance $r_{\max} = 4\,\text{mm}$, and the number of nodes in the support domain $N = 8$.

Figures 7 and 8 show the recorded E_z component at the observation point as a function of the frequency for the lossless and the lossy cases, respectively. The TE_{100}, TE_{010}, and TE_{110} resonance frequencies are summarized in Tables 1 and 2. By referring to the analytical resonance frequencies, we note that the relative error is clearly minimal for all the AOM modes in comparison with the axial optimization method, which in turn is more accurate than the RPIM.

All simulations were performed on AMD Athlon Dual Core Processor PC with a CPU of 2.61 GHz and 2 GB RAM.

Table 3 shows the computational time and memory requirements used in the lossless and lossy cases. For the lossy case, we find almost the same computational cost with a negligible CPU difference (lower than 1%) between the three methods. However, for the lossy case, one can note a small increase

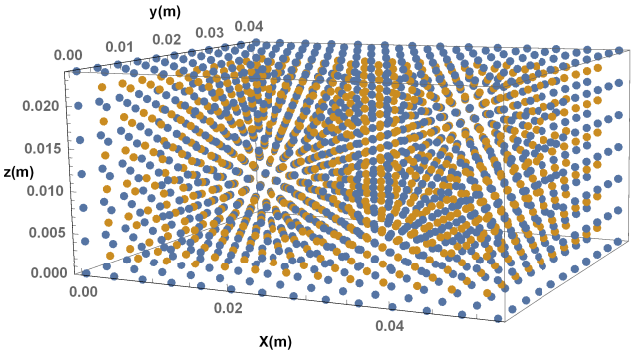

Figure 5. E/H node distributions in the rectangular cavity.

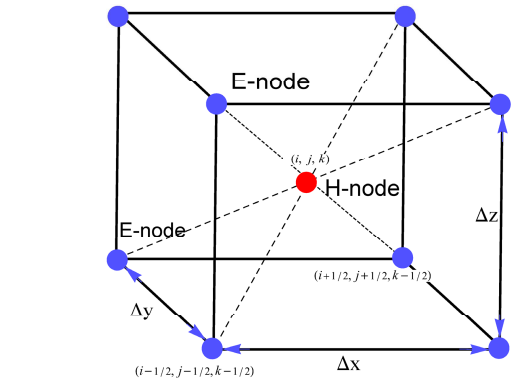

Figure 6. H-node support domain.

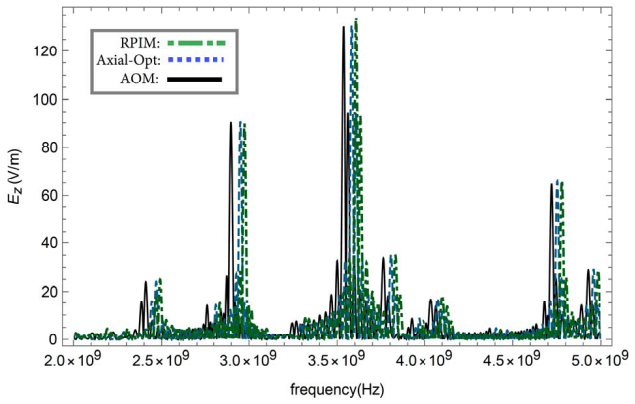

Figure 7. E_z component at the observation point of the rectangular cavity as function of frequency for lossless case. The simulation parameters are given in Table 1.

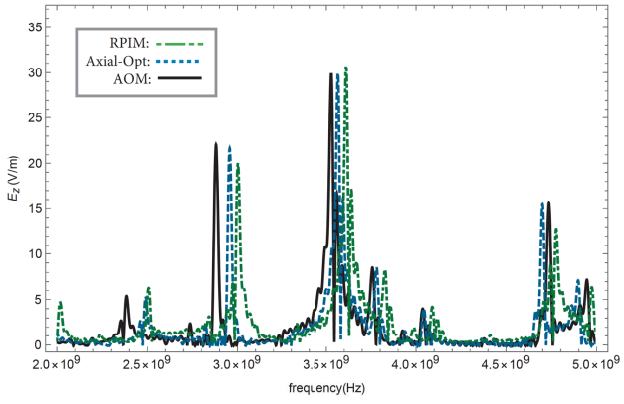

Figure 8. E_z component at the observation point of the rectangular cavity as function of frequency for lossy case. The simulation parameters are given in Table 2.

Table 1. Lossless case: Resonance frequencies given by RPIM, axial-optimized, and AOM-RPIM. $\sigma = 0\,\mathrm{S/m}$, $N_s = 20$ and $S = 0.5$.

Method	TE_{100}		TE_{010}		TE_{110}	
	Frequency (GHz)	Relative error	Frequency (GHz)	Relative error	Frequency (GHz)	Relative error
Analytic	2.884	-	3.75	-	4.731	-
RPIM	2.924	1.36%	3.935	4.95%	4.784	1.12%
Axial-Opt	2.913	1.01%	3.735	0.37%	4.763	0.68%
AOM	2.882	0.056%	3.756	0.17%	4.732	0.035%

Table 2. Lossy case: Resonance frequencies given by RPIM, axial-optimized, and AOM-RPIM. $\sigma = 0.001\,\mathrm{S/m}$, $N_s = 20$ and $S = 0.5$.

Method	TE_{100}		TE_{010}		TE_{110}	
	Frequency (GHz)	Relative error	Frequency (GHz)	Relative error	Frequency (GHz)	Relative error
Analytic	2.884	-	3.75	-	4.731	-
RPIM	3.022	4.7%	3.627	3.25%	4.791	1.28%
Axial-Opt	2.965	2.79%	3.788	1.03%	4.697	0.71%
AOM	2.880	0.15%	3.750	0.021%	4.735	0.082%

Table 3. Computational time and memory requirement in lossless and lossy cases for the rectangular cavity.

Method	Lossless case		Lossy case	
	CPU time (Seconds)	Memory (Mb)	CPU time (Seconds)	Memory (Mb)
RPIM	33.623	182.306	35.218	192.294
Axial-Opt	33.983	182.445	35.494	196.293
AOM	33.934	182.344	36.065	201.894

in the CPU and the memory used by the AOM compared to the RPIM. The relative increase in memory for the AOM is estimated to about 5%, which is always small and without significant consequences on the AOM performance.

6. CONCLUSION

In this paper, we have presented the algorithm of a 3D adaptive optimization method, which allowed us to cancel the numerical anisotropy for Cartesian grids. The derived algorithm can be easily adapted to the RPIM due to its flexibility. The shape functions are numerically calculated with the corresponding discretized adaptive factors at each node position. The obtained results deduced from the dispersion relation confirm that the accuracy is much greater using the AOM approach than with the conventional axial optimization technique. We have applied this AOM to 3D rectangular cavity resonator for lossless and lossy cases. A comparative study shows that the AOM accuracy for both cases is far from the conventional one since both numerical dispersion and loss are canceled. In summary, the NPE decreases from nearly 0.01 to 0.001 for the axial-opt-RPIM and completely vanishes for AOM-RPIM regardless of the ϕ values. For all the AOM modes, we have also obtained a minimal relative error in the resonance

frequencies, compared to previous methods.

Finally, note that the computationally-efficient AOM algorithm is relatively simple to implement in the RPIM, but its integration into other numerical mesh methods is not an easy task.

REFERENCES

1. Ciarlet, P. G., *Handbook of Numerical Analysis, Numerical Methods in Electromagnetics*, Vol. XIII, Elsevier, 2005.
2. Taflove, A. and S. C. Hagness, *Computational Electrodynamics: The Finite-Difference Time-Domain Method*, Artech House, 2000.
3. Liu, G. R. and Y. T. Gu, *An Introduction to Meshfree Methods and Their Programming*, Springer, 2005.
4. Kaufmann, T., Y. Yu, C. Engström, Z. Chen, and C. Fumeaux, "Recent developments of the meshless radial point interpolation method for time-domain electromagnetics," *Int. J. Numer. Model.*, Vol. 25, 468–489, 2012.
5. Kaufmann, T., C. Engström, and C. Fumeaux, "Residual-based adaptive refinement for meshless eigenvalue solvers," *International Conference in Electromagnetics on Advanced Applications*, 244–247, IEEE, Sydney, Australia, 2010.
6. Alaa, G., E. Francomanob, A. Tortoricib, E. Toscanob, and F. Violaa, "Smoothed particle electromagnetics: A Mesh-free solver for transients," *Journal of Computational and Applied Mathematics*, Vol. 191, 194–205, 2006.
7. Schweitzer, M. A., *A Parallel Multilevel Partition of Unity Method for Elliptic Partial Differential Equations*, Springer, 2003.
8. Atluri, S. N. and S. Shen, "The Meshless Local Petrov-Galerkin (MLPG) method: A simple & less-costly alternative to the finite element and boundary element methods," *CMES*, Vol. 3, No. 1, 11–51, 2002.
9. Juntunen, J. S. and T. D. Tsiboukis, "Reduction of numerical dispersion in FDTD method through artificial anisotropy," *IEEE Transactions on Microwave Theory and Techniques*, Vol. 48, No. 4, Apr. 2000.
10. Wang, S. and F. L. Teixeira, "Dispersion-relation-preserving FDTD algorithms for large-scale three-dimensional problems," *IEEE Trans. on Ant. and Prop.*, Vol. 51, No. 8, 1818–1828, Aug. 2003.
11. Nehrbass, J. W., J. O. Jevtic, and R. Lee, "Reducing the phase error for finite-difference methods without increasing the order," *IEEE Trans. on Ant. and Prop.*, Vol. 46, No. 8, 1194–1201, Aug. 1998.
12. Cole, J. B., "A high-accuracy realization of the Yee algorithm using non-standard finite differences," *IEEE Transactions on Microwave Theory and Techniques*, Vol. 45, 991–996, Jun. 1997.
13. Forgy, E. A. and W. C. Chew, "A time-domain method with isotropic dispersion and increased stability on an overlapped lattice," *IEEE Trans. on Ant. and Prop.*, Vol. 50, 983–996, Jul. 2002.
14. Yu, Y. and Z. Chen, "A 3-D radial point interpolation method for meshless time-domain modeling," *IEEE Transactions on Microwave Theory and Techniques*, Vol. 57, No. 8, 2015–2020, Aug. 2009.
15. Lee, J. F., R. Lee, and A. Cangellaris, "Time-domain finite-element methods," *IEEE Trans. on Ant. and Prop.*, Vol. 45, No. 3, 430–442, Mar. 1997.
16. Naamen, H. and T. Aguili, "Unconditional stability analysis of the 3D-radial point interpolation method and Crank-Nicolson scheme," *Progress In Electromagnetics Research M*, Vol. 68, 119–131, 2018.
17. José, A. P., G. Ana, G. Oscar, and V. Angel, "Analysis of two alternative ADI-FDTD formulations for transverse-electric waves in lossy materials," *IEEE Trans. on Ant. and Prop.*, Vol. 57, No. 7, 2047–2054, Jul. 2009.
18. Naamen, H., A. B. H. Hamouda, and T. Aguili, "Anisotropy analysis of the 3D-radial point interpolation method in lossy media," *Progress In Electromagnetics Research C*, Vol. 128, 207–218, 2023.

19. Harrington, R. F., *Time Harmonic Electromagnetic Fields*, IEEE Press Series on Electromagnetic Wave Theory, Wiley-Interscience, 2001.
20. Koh, I. S., H. Kim, J. Mi. Lee, J. G. Yook, and C. S. Pil, "Novel explicit 2-D FDTD scheme with isotropic dispersion and enhanced stability," *IEEE Trans. on Ant. and Prop.*, Vol. 54, No. 11, Nov. 2006.
21. Fu, W. and E. L. Tan, "Stability and dispersion analysis for ADI-FDTD method in lossy media," *IEEE Trans. on Ant. and Prop.*, Vol. 55, No. 4, Apr. 2007.
22. Pozar, D. M., *Microwave Engineering*, 3rd Edition, Wiley, New York, 2005.